Surface & Coatings Technology 493 (2024) 131278

Contents lists available at ScienceDirect

Surface & Coatings Technology

journal homepage: www.elsevier.com/locate/surfcoat

Full length article

Investigation of the cooling hole blockage induced by different thermal spray TBC deposition processes

Martin Rüßmann [a,*], Emine Bakan [a], Susanne Schrüfer [b], Olivier Guillon [a,c], Robert Vaßen [a,d]

[a] Forschungszentrum Jülich GmbH, Institute of Energy Materials and Devices (IMD), Material Synthesis and Processing (IMD-2), 52425 Jülich, Germany
[b] Materials Engineering, Rolls-Royce Deutschland, 15827 Blankenfelde-Mahlow, Germany
[c] Jülich Aachen Research Alliance (JARA-Energy), 52425 Jülich, Germany
[d] Institut für Werkstoffe, Ruhr-Universität Bochum, Bochum, Germany

ARTICLE INFO

Keywords:
Additive Layer Manufacturing
Cooling holes
TBC
Thermal Spraying

ABSTRACT

High-temperature turbine airfoils and combustion chamber walls in jet engines require sufficient cooling via cooling holes and thermal barrier coating systems (TBCs) to protect them from hot combustion gases. As the demand for greater efficiency and higher firing temperatures in jet engines increases, there is a corresponding need for more advanced film cooling methods, such as the use of more complex hole geometries. The use of Additive Layer Manufacturing (ALM) techniques allows the production of such intricate cooling holes, enhancing the flow of cooling air onto component surfaces. Conventional TBC deposition techniques, for example Atmospheric Plasma Spraying (APS) or Electron Beam Physical Vapor Deposition (EB-PVD), often lead to partial or complete blockage of cooling holes. This study compares the blockage of TBCs deposited on conventionally-sheet alloys with standard cooling holes and ALM alloys with more complex cooling holes using APS as a baseline process. Additionally, alternative plasma spray deposition technologies such as Suspension Plasma Spraying (SPS) and Plasma Spray-Physical Vapor Deposition (PS-PVD) were explored. The aim was to determine the effectiveness of these processes in preventing blockage compared to the traditional APS process. The experimental results showed that the formation of the coating, whether originating from splats or from the vapor phase, the feedstock particle size, and the cooling hole geometry can all affect the blockage. It was demonstrated that PS-PVD, with its vapor-induced deposition, is highly effective in minimizing blockage, regardless of the cooling hole geometry.

1. Introduction

For decades, aeronautical research has aimed to achieve higher turbine inlet temperatures, increased efficiencies, and reduced emissions from jet engines [1]. This pursuit necessitates both advanced materials of thermal barrier coatings and improved film cooling. For component film cooling, a laser-drilled cooling hole system enables a continuous flow of cold air along the hot surface, resulting in a protective air film [2]. New Additive Layer Manufacturing (ALM) techniques, such as Direct Metal Laser Melting (DMLM) enable the manufacturing of complex shaped parts [3,4] including cooling hole structures designed to prevent blockage during deposition. This is a challenge with traditional casting methods. Ideally, the cooling channels should be designed with a shallow angle, ensuring that the cold air flow remains on the surface when exiting the cooling hole. Furthermore, disadvantageous blocking by deposition of particles, such as dust, sand and volcanic ash must be prevented [5–7]. This is crucial as any form of blockage can lead to deflection of the cooling air flow, resulting in increased surface temperatures of the TBCs [6]. Before installation into the combustion chamber or turbine, it is therefore critical to ensure an absolute minimum cooling hole blockage after coating deposition. Usually, a laser is used to drill the cooling holes after deposition of the coatings or the holes are reopened mechanically after the deposition of the TBC systems [8,9]. However, this can result in flaws in the coatings such as spattering, delamination, or micro-cracking [10,11]. Post-machining after TBC deposition can be considered a necessary but cumbersome step in turbine component manufacturing. As a result, there is a growing demand for innovative solutions that can eliminate these time-consuming steps.

* Corresponding author.
E-mail address: m.ruessmann@fz-juelich.de (M. Rüßmann).

https://doi.org/10.1016/j.surfcoat.2024.131278
Received 28 May 2024; Received in revised form 19 August 2024; Accepted 19 August 2024
Available online 29 August 2024

1.1. Thermal spray processing of TBCs and its influence on cooling hole blockage

TBC systems consisting of a rough metallic bond coat (BC) for enhanced adhesion and oxidation protection [12–15] and a ceramic top coat (TC) deposited by thermal spraying [16,17] are considered here. Thermal spray processes, which employ combustion or plasma generation, are utilized to deposit thermal barrier coatings (TBCs) [18]. As the material is then injected into the gas stream, it is accelerated, heated and typically melted [18]. The semi-molten particles or molten droplets impact the substrates and form splats that progressively deposit and build-up a coating [18]. Due to the nature of substrate cooling holes, off-normal particle impacts are inevitable. The spraying angle, particle state, and potential deflection due to impact on inclined surfaces all contribute to cooling hole blockage. This effect is also dependent on the specific thermal spray process used.

The metallic bond coats can be thermally sprayed, e.g. by HVOF, where the combustion of a fuel/gas mixture provides the energy to heat the MCrAlY (M = Ni, Co + Ni, Fe) alloy powder. The feedstock after injection into the hot gases can be accelerated to supersonic speed by traveling through a convergent-divergent de Laval nozzle [18]. Upon impact with the substrate, the softened material peens, deforms and results finally in a highly dense coating [18,19].

The top coat layer comprises a thermal insulating layer of ~7–8 wt% yttria stabilized zirconia (YSZ). The most traditional thermal spray process to deposit YSZ has been APS. In APS, relatively coarse powder particles with a diameter ranging from 10 to 150 μm are injected radially into a plasma gas stream that is typically composed of argon and hydrogen or argon and helium [18]. These particles can melt into large droplets that impinge on the substrate forming splats [18]. It is well-known that APS is a line-of-sight deposition process that can obstruct e.g., cylindrical and shaped cooling holes [20].

In recent years, efforts have been made to improve the robot programming, trajectories, and process kinematics in order to obtain a homogeneous coating on complex-shaped substrates [21]. This includes a better control over spray velocity, spray distance, spraying angles, and spray paths for optimized heat and mass transfer to the substrate [21]. This is attempted by advanced robot programming tools that utilize CAD models of the substrate or that couple with Computational Fluid Dynamic (CFD) simulations [22,23]. These concepts have been successfully tested on large, complex-shaped components, such as a ship's propeller [24]. An optimized spray path may also reduce the blockage of holes by adjusting the spraying angles. However, it is not possible to avoid material entering the holes, given that the diameter of the holes is in the range of a few millimeters, as well as the distance to neighboring holes. Line-of-sight deposition processes, such as APS or HVOF [18], are characterized by the presence of expanding gas flows with dispersed particles, which give rise to spray spots with a diameter of a few tens of millimeters. This would be a considerably larger diameter in comparison to the dimensions of the holes.

To prevent the blockage, non-line of sight thermal spray processes, including SPS and PS-PVD, can be suitable tools [25–27]. As an alternative to traditional plasma spraying, SPS may offer the advantage of decreased susceptibility to cooling hole blockage, as the submicron sized particles injected to the plasma can follow the jet streamlines and the trajectories can be potentially influenced by adjusting the particles inertia and the drag of the gas jet. Tang et al. [28] investigated the potential of SPS to prevent blockage of cooling holes in airfoils. The results showed that the cooling holes remained open with minimal blockage after deposition. Bernard et al. [29] used SPS to coat a high-pressure turbine blade with cooling holes. They found little blockage, except for some YSZ residues within the cooling holes, which could be removed by high-pressure compressed air. The dimensionless Stokes number (Eq. (1)) may explain these findings. It represents the characteristic time ratio for momentum transfer of a particle or droplet to adjust to the flow [30]. So, it can determine whether the particle can follow the gas flow and potentially avoid the blockage of the cooling holes.

$$St = \frac{\rho_p \cdot {d_p}^2 \cdot v_p}{\mu_g \cdot \delta_{BL}} \quad (1)$$

with ρ_p = Density of the particle, d_p = particle diameter, v_p = velocity of the particle, μ_g = viscosity of the plasma gas, δ_{BL} = gaseous boundary layer thickness.

The situation is illustrated in Fig. 1, where a plasma gas flow with axially injected particles impacts perpendicularly on a flat substrate. As a result, it decelerates and comes to a stop in front of the substrate [30,31]. This creates a stagnation point at the point of impact, where the static pressure is at its maximum and the axial velocity of the gas flow is zero [32,33]. Therefore, only particles with enough momentum ($St > 1$) can enter this stagnation zone and deposit perpendicularly to the surface, as shown in Fig. 1. The static pressure decreases radially [33,34] as the gas flow is deflected, enabling particles with $St < 1$ to follow the deflected gas flow and increase their radial velocity [30,35]. They either deposit on asperities with a shallow angle and contribute to the growth of the columns or do not deposit at all [30].

Additionally, a thin gaseous boundary layer forms on the surface due to the viscosity of the gas flow and the friction effects between the fluid and the surface [36]. The velocity of the jet returns to the freestream velocity as the shear stress decreases along the surface [36]. The thickness of this boundary layer (δ_{BL}) is defined as the point where the jet returns to 99 % of the freestream velocity [36]. The particles' Stokes number must also be greater than one to cross the boundary layer and reach the substrate [17].

To reduce the Stokes number (Eq. (1)) and deflect particles, one can decrease particle size or particle velocity, which is related to the gas flow velocity. The drag force (F_D) defined in (Eq. (2)) can significantly impact the velocity of particles by causing deceleration near the substrate, which may result in lower Stokes numbers. The drag force can vary depending on the shape of the substrate, whether it is flat (with or without cooling holes) or cylindrical. The shape of the substrate has an impact on the formation of the stagnation zone and the resulting drag force [32,33]. While a cylindrical substrate results in a lower drag force and a smaller stagnation zone, particles are less likely to deposit on it compared to a flat substrate [32,33]. This is due to the formation of the boundary layer around the cylindrical substrate, which causes particles with low Stokes numbers to flow around it.

$$F_D = C_D \cdot A \cdot \frac{\rho \bullet v^2}{2} \quad (2)$$

with C_D = drag coefficient of the flow, A = Reference area, ρ = Density of the fluid, v = Velocity of the gas flow relative to the object.

In their study, Kielczawa et al. [37] investigated the effect of topography on boundary layer formation in SPS. They used V-shaped and rectangular textured surfaces and found significant local pressure fluctuations in the surface structures located in the outer regions of the substrate. In these areas of local stagnation, the plasma gas swirled, and the particles were deposited in the low-pressure regions. This phenomenon is likely to occur on substrates with cooling holes. To further lower the Stokes number, it is beneficial to use also high-power plasma gas flows with a high percentage of argon and/or helium to increase the gas flow viscosity. This is because the viscosity increases with temperature up to 15,000 Kelvin for argon and 20,000 Kelvin for helium [18]. Additionally, it is important to ensure a thick boundary layer thickness. This is because only particles with enough momentum can pass through it and block the cooling holes. According to [18], the boundary layer thickness is inversely proportional to the square root of the flow velocity and depends on factors such as the nozzle design, gas flow rate, and spray distance.

As a second alternative for APS, the PS-PVD process combines the benefits of two technologies: EB-PVD and plasma spraying. This process

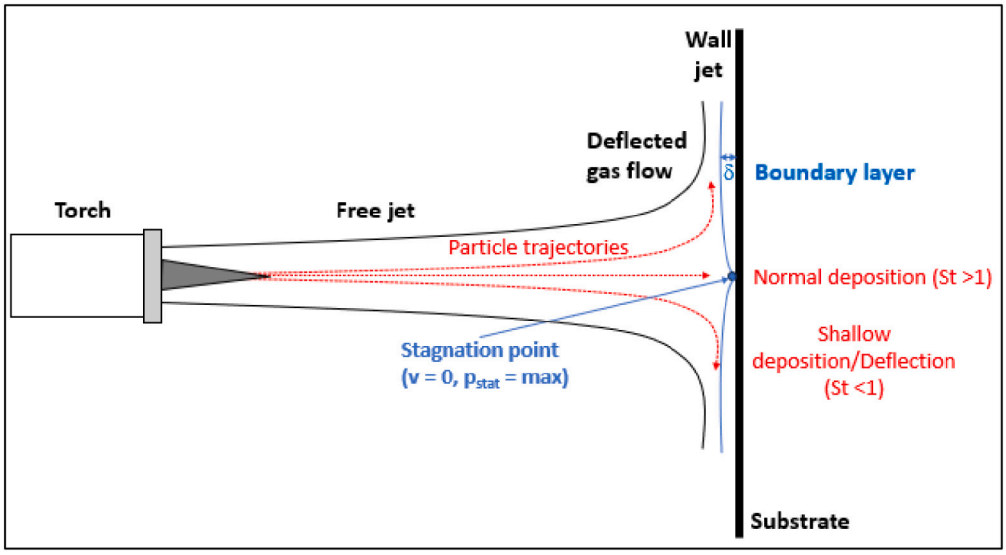

Fig. 1. Gas flow impacting perpendicularly on the substrate (also called stagnation point flow/Hiemenz flow).

yields columnar structures similar to those seen in EB-PVD, but with the added advantages of higher deposition rates and potential cost savings relative to EB-PVD [38]. In PS-PVD, a fine powder feedstock with a particle size range of 1 to 30 μm is injected into a high power (up to 180 kW) plasma jet at a low working pressure (≤2 mbar), causing the particles to melt and even evaporate completely before deposition [39–41]. The deposition can occur by condensation of the evaporated species in the boundary layer of the substrate, where supersaturation is likely [30]. Additionally, spherical particles that did not evaporate but instead melted and resolidified can also be present in the coatings [42]. With long spray distances and a high degree of evaporation, columnar-feathery like structures can be achieved [30]. As the material in the vapor phase is transported within the stream it can deposit in areas accessible by the plasma [38]. This enables the coating of non-line-of-sight areas, including complex geometries such as multiple turbine air foils or double vanes [39]. Additionally, it permits the deflection of the gas flow in front of the cooling holes, thus preventing their blockage. This was successfully tested on engine components [44].

This study seeks to both qualitatively and quantitatively compare and evaluate the blockage behavior of the spray processes that can be used to fabricate a TBC system. Key process factors that contribute to blockages are examined, along with how these factors are influenced by different cooling hole geometries.

2. Materials and methods

2.1. Substrates

One of the substrates utilized in this study were nickel-based, solid solution strengthened Haynes®230® Ni-base alloys, containing elements such as Cr, W, and Mo. These substrates were additively manufactured through the process of Direct Metal Laser Melting, to a final square geometry that measured 50 × 50 × 1.2 mm^3. Subsequently, sections of 25 × 25 mm^2 were cut for the spray experiments. The cooling

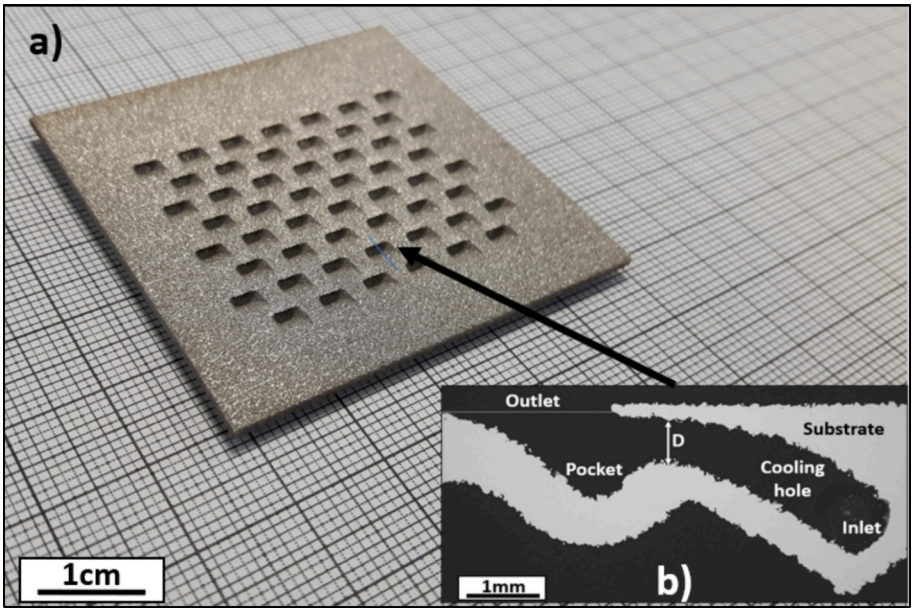

Fig. 2. a) ALM Substrate with cooling holes and b) SEM image of a cooling hole cross section with theoretical inlet and outlet for the cooling air flow and a pocket structure marked with a red box. D = minimum diameter of the hole.

holes, as displayed in Fig. 2a) and b), were not continuous, and instead closed at the back side (inlet). The ratio of the outlet area to the inlet area of the hole is approximately 7:1, with a minimum diameter (D) of the hole of 0.5 mm. They also had a "pocket" structure (Fig. 2b)) to prevent blockage during deposition at the cooling air outlet. The structure can be filled with material in such a way that it does not impede the entry of the inner cooling hole area. This allows for an unobstructed transfer of the cooling air flow towards the hot surfaces outside the holes. Conversely, the cooling air can become disturbed and form unwanted turbulences in this area when the structure is not properly filled.

For comparison purposes, Sheet C263® nickel-base alloys with continuous fan-shaped cooling holes were coated, as depicted in Fig. 3. The ratio of the inlet to outlet area was here 2:1, with a minimum diameter D of 0.8 mm. These were gamma-prime precipitation hardening alloys with solid solution strengthening elements, including chromium, cobalt and molybdenum. The substrates were also cut into segments measuring 25 × 25 × 1.5 mm^3 for the spray experiments. To enhance bond coat adhesion, these substrates underwent grit blasting with F36 corundum at 2.5 bar and ultrasonic cleaning in ethanol after grit-blasting. During the grit blasting process, the substrate was held at an angle to prevent blasting into the holes. This was done to avoid the need for additional protection of the holes with wax or resin. After cleaning, the holes were inspected for grit and removed with compressed air or a metal wire if necessary. The surface roughness was measured using a stylus profilometer (MarSurf XR20, Mahr GmbH, Göttingen) with a cut-off wavelength (λc) of 2.5 mm. The ALM substrates from Fig. 2 were inherently rough and did not require additional grit-blasting. This is described in further detail later.

2.2. Bond coats

For the bond coat deposition, the CoNiCrAlY powder Amdry 9954 (Oerlikon Metco, Wohlen, Switzerland) was utilized with a particle size ranging from 11 to 63 and a d_{10} value of 20 µm, d_{50} value of 30 µm and d_{90} value of 44 µm. The particle size distribution was measured by static light scattering using a LA950 device (Horiba, Japan).

A six-axis robot (ABB IRB2400, Zurich, Switzerland) equipped with a DJ2600 Gas fuel HVOF spray gun (Oerlikon Metco, Wohlen, Switzerland) was used to spray the powder. The process gases were a mixture of hydrogen and oxygen with nitrogen used as shroud gas. The spray distance was set to 200 mm and aimed at the center of the substrate. The spray parameters are summarized in Table 1. To avoid spraying directly into the cooling holes and further hole protection steps, the spray angle was set at 79° by adjusting the tilt of the sample table as shown in Fig. 4. The 79°-spraying angle was chosen based on pre-experiments that studied the HVOF blockage propensity and was applied to both types of substrates. The bond coat thickness was targeted to be within a thickness range of 150–200 µm. For the PS-PVD process, the bond layers were deliberately sprayed thicker because the surfaces had to be polished to an Ra value of <2 µm prior to PS-PVD deposition. This was to ensure a homogeneous columnar microstructure with uniformly grown columns [43].

2.3. Plasma spraying deposition for top coats

Three different spraying methods were utilized for applying the YSZ top coats with corresponding parameters outlined in Table 2. For all the TC processes a 90° spraying angle was used.

a) APS

The TriplexPro 210 torch (Oerlikon Metco, Wohlen, Switzerland) was used to spray the standard APS YSZ top coats. For this an Argon-Helium plasma was used. The utilization of helium as a secondary gas instead of hydrogen, was undertaken to circumvent the potential for excessive particle melting, which could otherwise be facilitated by the high thermal conductivity of hydrogen [18] and result in a denser microstructure. The feedstock material selected was the 7–8 wt% partially stabilized YSZ powder Metco 204NS (Oerlikon Metco, Wohlen,

Table 1
Spray parameters HVOF.

Spray parameter	HVOF
Process gases	H_2, N_2, O_2
Gas flow rate (slpm)	630/460/165
Stand-off distance (mm)	200
Powder feed rate (g/min)	40
Spraying angle (°)	79

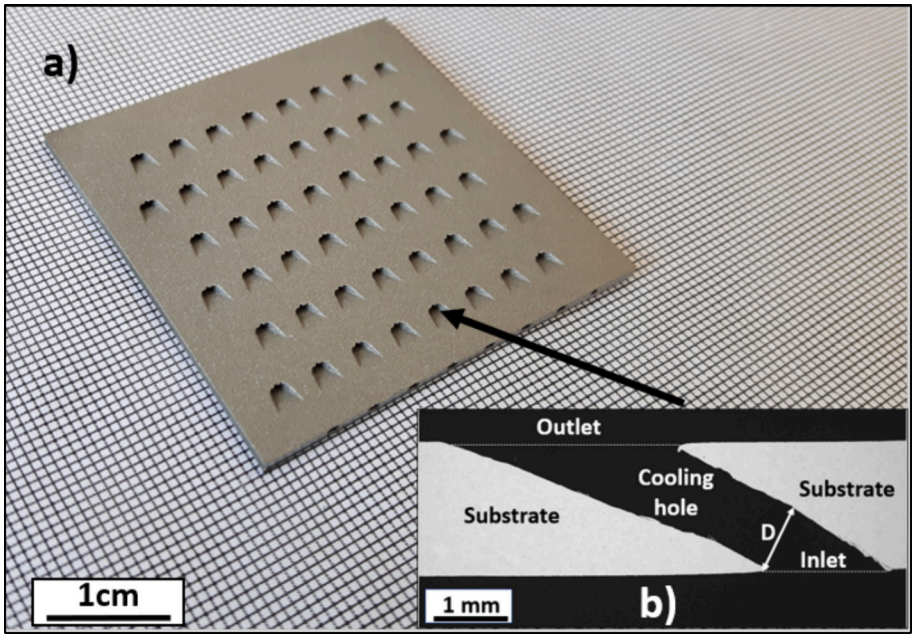

Fig. 3. a) Sheet C263 alloy with cooling holes b) SEM image of a cooling hole cross section.

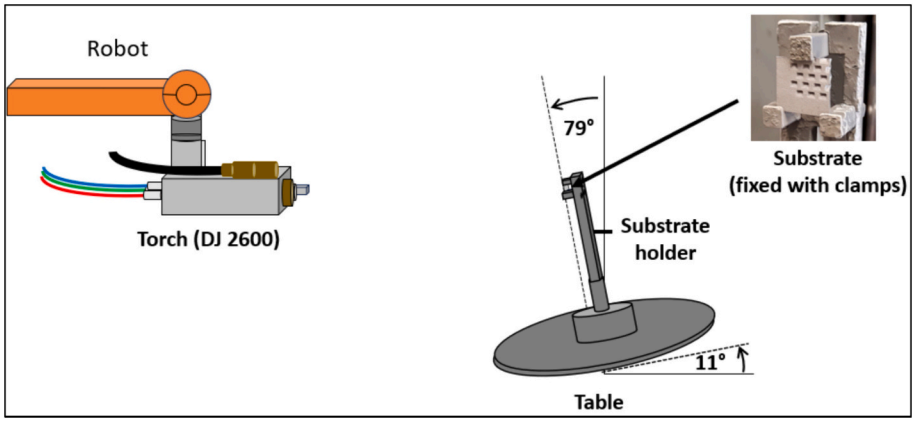

Fig. 4. Schematic set-up of the HVOF experiment.

Table 2
Overview of the used spray parameters of the different top coats.

Spray parameter	APS	SPS	PS-PVD [40]
Plasma gases	Ar-He	Ar-N_2-H_2	Ar-He
Gas flow rate (slpm)	46/4	225/30/45	35/60
Stand-off distance (mm)	200	70	1000
Environment	Ambient	Ambient	2 mbar (chamber pressure)
Net power (kW)	22	43	60
Powder feed rate (g/min)	29	13	2 × 8
Cooling conditions	Front	Back	–

Switzerland), with a particle size distribution between 11 to 125 µm and a d_{10} value of 30 µm, d_{50} value of 56 µm and d_{90} value of 91 µm. A front side cooling using air jets with four bar pressure was simultaneously employed during spraying.

b) SPS

The spray gun used for the SPS top coats was an Axial III™ gun from Mettech (Northwest Mettech Corp., North Vancouver, Canada). The YSZ-suspension utilized in this study was produced by Treibacher AG (Althofen, Austria). The suspension was initially composed of a 40-weight percent solid load and was subsequently diluted with ethanol to 25 wt%. The suspension was diluted due to the tendency of the original 40-weight percent suspension to clog the capillary used for spraying the suspension. Particles in the suspension had a d_{10} value of 72 nm, d_{50} value of 127 nm and a d_{90} value of 230 nm. It was fed using the commercial NanoFeed 350 liquid delivery system (Northwest Mettech Corp., North Vancouver, Canada) and axially injected into a plasma gas flow, which comprised of argon, hydrogen and nitrogen. A back-side cooling of 2.5 bar was used during spraying.

c) PS-PVD

The PS-PVD coatings were applied using a Oerlikon Metco LPPS-TF Multicoat system (Oerlikon Metco, Wohlen, Switzerland). The working pressure during spray deposition was maintained at approximately two millibars. A single cathode O3CP torch (Oerlikon Metco, Wohlen, Switzerland) was used with an Argon-Helium plasma gas mixture to deposit the coatings. The commercial YSZ feedstock used was Metco 6700 (Oerlikon Metco, Wohlen, Switzerland). The particle size range was between 1 and 30 µm with a d_{10} value of 2 µm, d_{50} value of 8 µm and d_{90} value of 18 µm [40]. The powder was injected into the nozzle radially by dual injection with two simultaneous powder hoppers. Prior to spraying, the bond coats were polished using an automated grinding and polishing machine (ATM Saphir 550, ATM Qness GmbH, Mammelzen, Germany). The surface roughness was quantified using a stylus profilometer, resulting in an average Ra value of less than two microns. The bond coat surface was oxidized during pre-heating via the additional flow of oxygen before the ceramic top coat was sprayed. The bond coat oxidizes forming an alumina layer that provides a good adhesion to the oxide ceramic, thereby limiting also interdiffusion between the bond coat and the top coat as described in [45]. This, in turn, enhances the thermal cycling lifetime [45,46]. The spray parameters used in this study were taken from reference [40] and are listed in Table 2.

2.4. Metallographic preparation

Cross sections of the samples were prepared for subsequent microstructural analysis. The samples were vacuum embedded using the two-part epoxy resin Epoxy 2000 (Cloeren Technology GmbH, Wegberg, Germany). Then the embedded samples were cut using an automatically fed cutting machine Discotom 100 (Struers GmbH, Ballerup, Denmark). After cutting, the specimens were mechanically ground and polished using standard metallographic polishing methods. To ensure that the cross-sections were located at the center point of the plane of the cooling holes, a manual hand-grinding step preceded the final polishing.

2.5. Microstructure analysis

Scanning Electron Microscopy (SEM) analysis was done by using a Hitachi TM3000 tabletop scanning electron microscope (Hitachi, Tokyo, Japan). Ten SEM images were captured at the same 150× magnification to assess the thickness of the coating across the entire surface. Using the open-source image analysis software ImageJ, the lowest and highest thickness of the TC were measured in each image and then the arithmetic mean for each image was calculated. The margin of error was calculated using the standard deviation.

2.6. Cooling hole blockage evaluation

The blocked hole area was evaluated via cross sections at a low (40×) magnification, as shown in Fig. 5. From the images, the coating material area inside the cooling hole was compared to the uncovered cooling hole area, as given in Eq. (3). Two cooling holes per sample were analyzed, and the mean value was calculated for the blocked area. Here again ImageJ was used for the measurement. For longer deposition runs or spray parameters with higher deposition efficiency for the same number of deposition runs, it can be inferred that the blocked hole area would increase due to the overall increase in thickness. Consequentially, from sample to-sample there would be an inconsistency. To account for this, the blocked hole area was divided by the average coating thickness of the BC and TC throughout the entire cross section, resulting in a blocking ratio, which is given in Eq. (4). This blocking ratio serves as the quantitative assessment by which the different spray processes and their

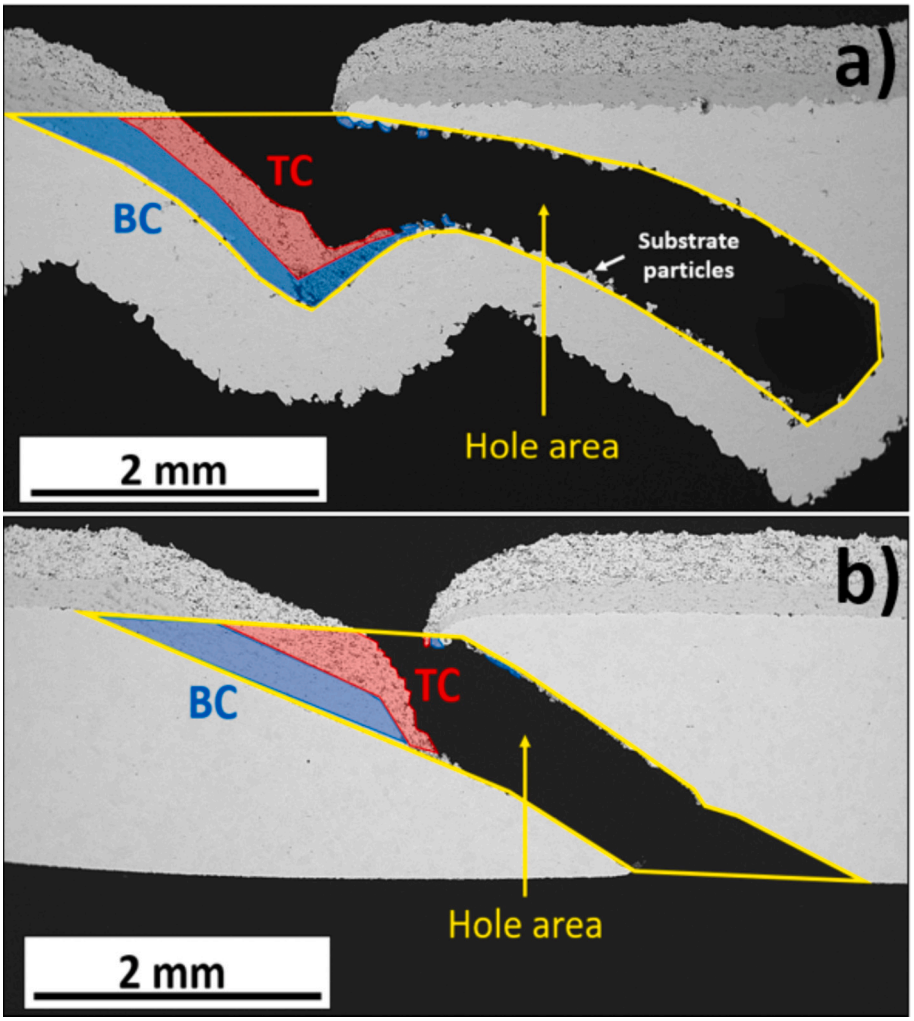

Fig. 5. Example of an SEM image of an ALM cooling hole (a) and a cooling hole from the sheet substrate (b), after spraying which was used to determine blockages. The purpose of the image was to identify the blockage of the hole area (yellow) by the bond coat (BC, blue) and the top coat (TC, red).

susceptibility to cooling hole blockage will be compared.

$$\text{Blocked hole area} = \frac{\text{Coating material } (\text{mm}^2)}{\text{Hole area } (\text{mm}^2)} \left(\%\right) \quad (3)$$

$$\text{Blocking ratio (BR)} = \frac{\text{Blocked hole area}}{\text{Avg.coating thickness}} \left(\frac{\%}{\mu\text{m}}\right) \quad (4)$$

The error of the blocking ratio was determined by the Gaussian error propagation law with summation of the relative errors.

2.7. Porosity determination

The porosity was quantified by image analysis using the software ImageJ on ten SEM images captured at 1000× magnification. Bandpass filtering and thresholding were employed to differentiate between the porosity and the surrounding material. For the columnar structured SPS and PS-PVD top coats, the inter-columnar gaps were incorporated into the porosity values. The coarse and fine porosity were summarized as a total porosity value.

3. Results and discussion

3.1. Surface topography prior to deposition

The ALM sample surface exhibited a high roughness, illustrated in Table 3, which appears to be due to the manufacturing process. It is possible that during the Direct Metal Laser Melting process, spherical particles of the nickel-based alloy were not completely melted by the laser beam, leading to their entrapment within the solidifying melt pools. These unmelted particles on the surface are generally considered as defects in laser-based processing methods [47,48]. The surface roughness of the C263 alloy that underwent grit-blasting was lower compared to that of the ALM sample.

Table 3
Roughness values on the flat areas outside the holes obtained from the stylus profilometer MarSurf XR20.

Roughness	Ra (μm)	Rz (μm)
ALM	13 ± 1	76 ± 3
Sheet (after grit-blasting)	3.3 ± 0.2	24 ± 1

Due to the relatively high surface roughness of the ALM samples, they were not grit-blasted prior to deposition and only cleaned in an ultrasonic bath with ethanol. The rough surface of the ALM substrate was sufficient to facilitate adhesion of the HVOF bond coat.

3.2. Bond coat deposition and propensity for cooling hole blockage

To mitigate the HVOF-induced blockage, it was found that a lower spraying angle of 79° is beneficial. This angle was chosen so that the top

edge of the cooling hole provides a shadowing effect for the pocket structure (Fig. 6a)) and finally resulted into limited material filling of the pockets. As also can be seen in Fig. 6a) and c) the bond coat microstructure changes in the shadowed area of the pocket from a dense microstructure on the curved edge to a highly porous one in the center of the pocket. The pocket structure helped to prevent blockage in the outlet area, which had already occurred in the sheet sample. However, the bond coat material was transported into the inner hole area and deposited on the top edge for both hole geometries This is shown in Fig. 6b) for the ALM sample.

The changes in the microstructure can be attributed to the impact of the high-velocity jet on the inclined surfaces and the subsequent insufficient deformation of the particles. The spraying angle continuously changes from 79° outside the curved ALM cooling holes to approximately 60° near the pocket center. In contrast, the spraying angle for the sheet samples remained constant at 70° in the outlet area of the hole. It is known that the thickness of the coating decreases as the spraying angle decreases. As the tangential components of the particle's velocity vector increase, there is a higher probability of the particles not deforming completely or rebounding from the surface [49,50]. Beside the rebounding, it is also possible that splashing occurs for high velocity particles impacting on the surface, which could also explain the material that deposited at the top edge in the inner hole area. The occurrence of splashing is likely to occur for particles exhibiting high impact velocity, larger diameter, and elevated temperature [18], which are situated in the central region of the gas flow. The material found in the inner hole area is also only a few microns in size, which is smaller than the minimum particle size of the powder, which is approximately ten microns.

3.3. Top coat deposition and propensity for cooling hole blockage

The APS, SPS, and PS-PVD TBCs were deposited both on the ALM substrates with their specific hole geometry and on conventionally sheet C263 substrates with fan-shaped cooling holes for comparison. The average coating thickness of the bond coat and top coat and the average porosity values of the top coat are summarized in Table 4. The high porosity of the PS-PVD coatings results from the large inter-columnar gaps and feathery-like columnar microstructure.

A representative cooling hole cross section for each system is shown in Fig. 7.

The images show variations in blockage levels and areas of material deposition, especially in the pockets, the hole openings, the inner hole area, and the back side of the substrate. For quantitative evaluation of the blockage for both hole geometries and the used coating processes the blocking ratio based on Eq. (4) was used. The objective was to relate the area of the sprayed bond coat and top coat to the uncoated hole area to cover both the blockage at the hole opening and in the inner hole area, as was illustrated in Fig. 5. The uncoated hole area of the SEM image of the hole for the ALM substrate was, on average, 4.6 ± 0.1 mm^2, which was larger than the area of the sheet samples, which was 2.9 ± 0.5 mm^2. The greater deviation in the sheet samples can be attributed to the metallographic preparation process. This is due to the diameter of the hole appeared to be smaller, which makes it more challenging to grind and polish towards the center of the hole cross-section.

The results in Figs. 7 and 8 showed that the PS-PVD samples had the lowest amount of blockage. However, for APS and SPS the level of blockage seemed to have been influenced by the hole geometry. When comparing the images and the blocking ratio for the APS samples it can be found that the ALM samples were significantly less blocked compared to the sheet samples. The blocking ratio for the SPS samples was similar for the ALM and sheet samples. The error bars are also larger, because the SPS coating thickness varied more due to the different column sizes, as the growth occurred on different sized asperities on the bond coat surface. Nevertheless, the SPS coatings blocked the ALM samples more compared to APS as material was also deposited in the inner hole area, whereas it was less for the sheet sample.

The HVOF bond coats exhibited overall the highest blockage propensity for both hole geometries with a blocking ratio of 0.054 ± 0.008 %/µm on the ALM samples and 0.089 ± 0.009 %/µm for the sheet samples. It is important to note that the BR-values of the bond coats sprayed for the PS-PVD samples were not considered due to their higher values resulting from the inability to polish the bond coats within the

Table 4
Coating characteristics obtained from the coatings outside the holes.

Substrate		APS	SPS	PS-PVD
ALM	Coating thickness BC (µm)	233 ± 12	228 ± 21	228 ± 37
Sheet		190 ± 5	206 ± 16	266 ± 13
ALM	Coating thickness TC (µm)	319 ± 5	340 ± 13	285 ± 35
Sheet		298 ± 8	458 ± 12	215 ± 33
ALM	Porosity TC (%)	17 ± 1	13 ± 2	22 ± 1
Sheet		17 ± 1	11 ± 2	24 ± 1

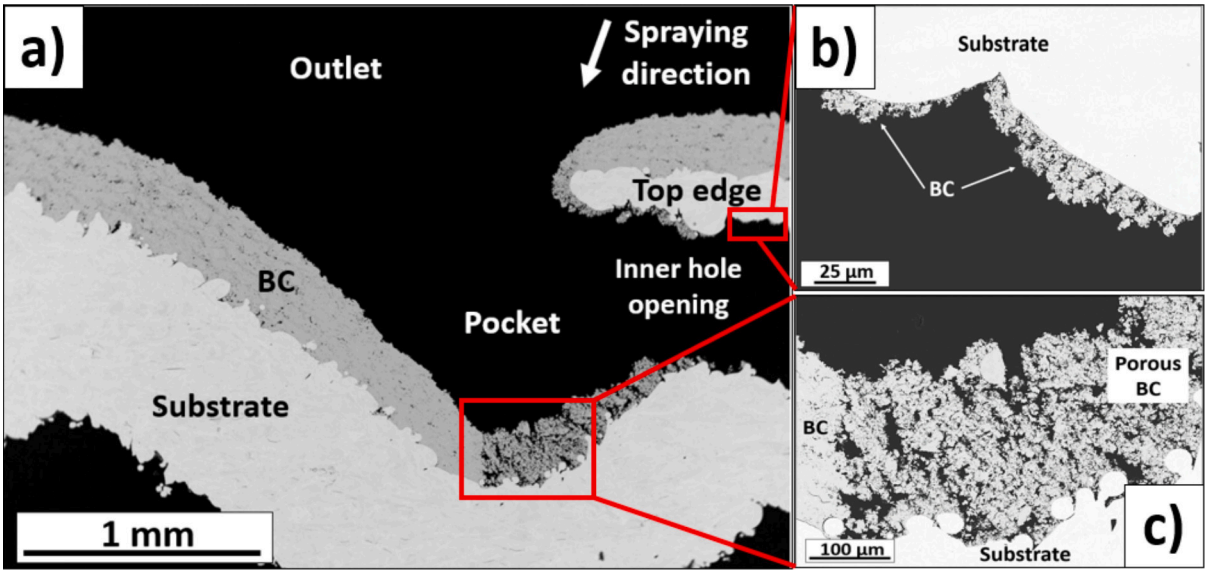

Fig. 6. a) Bond coat sprayed with 79° in ALM pocket structure in front of the cooling hole.
b) Small BC particles in the inner hole area c) Porous bond coat in the ALM pocket.

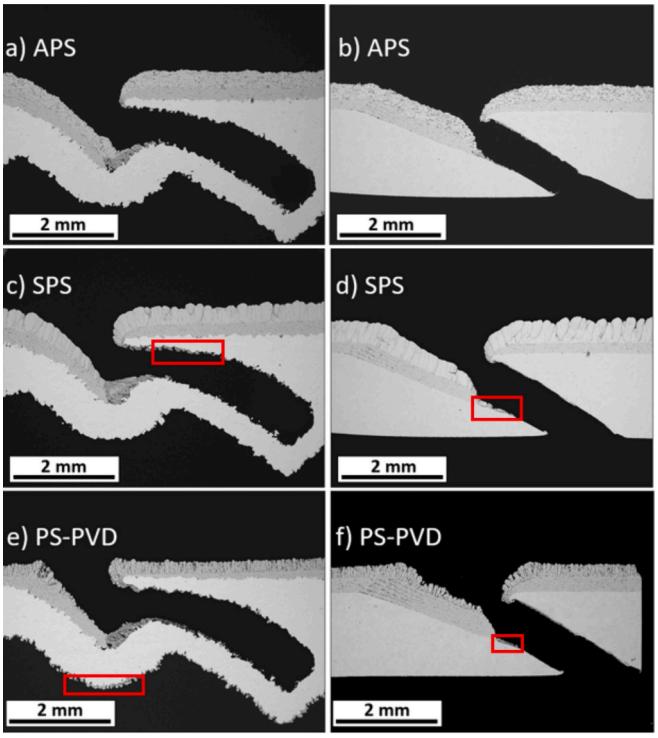

Fig. 7. The left column displays SEM cross sections of the cooling holes for the ALM substrate with a BC and the corresponding top coats, while the right column shows the same for the sheet substrate. c) and d) SPS TC in the inner hole area (marked with a red box) e) PS-PVD TC at the back surface of the sample (marked with a red box).

holes, as shown in Fig. 7e) and f).

The succeeding sections provide a more detailed description of the blockages, their respective locations, and microstructural characteristics. For that, the cooling holes were investigated in two area, the outlet area with the hole opening and the inner hole area.

a) Microstructure and cooling hole blockage from the APS process

The APS coatings filled the pockets of the ALM substrates up to the area that was shadowed by the top edge, as shown in Fig. 9a). The inner hole area remained unblocked by the APS sprayed material with most of the material resulting from the sprayed bond coats. Only a few smaller particles were transported into the inner cooling hole area as illustrated in Fig. 9b). In contrast, the APS coating sprayed on the sheet samples blocked the inner hole opening, as seen in Fig. 7b). The reason for this is that relatively large particles with high momentum, and therefore a large Stokes number, could not follow the deflected gas flow in front of the substrate. As a result, the particles were deposited mostly in a line-of-sight manner, specifically in the outlet area up to the inner hole opening.

b) Microstructure and cooling hole blockage from the SPS process

The SPS coatings on the flat surfaces of the sample showed a columnar structure, with the columns growing perpendicular to the substrate surface. In the outlet area of the cooling holes, the spray angle gradually changed from 90° to 46° towards the center of the pocket due to the curvature of the substrate, also given in Table 5. Consequently, the growth angle of the SPS columns also changed from 90° to approximately 59° relative to the bond coat surface. The growth of columns in a plasma jet is typically parallel to the spray direction due to the influence of particle momentum, plasma drag, and spray angle [51–53]. The diameter of the plasma jet is larger than that of the cooling holes. This causes deposition to occur from particles deflected into the cooling holes traveling on different trajectories in the center or on the fringes of the jet. Additionally, the height of the columns decreased by 60 % from the hole entry to the center of the pocket, which correlated with a decreasing growth angle, as shown for the ALM substrate in Table 5. This could be explained by the changed shadowing conditions, as the columns at higher positions capture more particles than those further down the hole. Particles deflected from the top edge of the cooling holes may contribute to the growth of the coating in the outlet area, leading to blockage. This is also shown for the sheet samples in Table 5 and Fig. 11, where the columns change their growth angle as the shadowing effect of the right side of the cooling hole increases.

In the center of the pocket there was a change to a microstructure consisting of porous layers composed of resolidified/unmolten spherical particles with vertical cracks (relative to the substrate surface) propagating through the layers, as shown in Fig. 10a) and c). These porous layers alternated with layers of molten particles. On the right side of the pocket, seemed to be shallow grown columns with spherical particles accumulating in the gaps between the columns. The high number of spherical particles in the center of the pocket may be due to the droplets with a high solid loading of particles that have not completely melted. In addition, shadowing effects from the edges and turbulences in the concave pocket structure may lead to the layered deposition of material in the center.

As shown in Fig. 10a) and b), mainly sub-micron-sized partially melted or unmelted particles with a low Stokes number could follow the

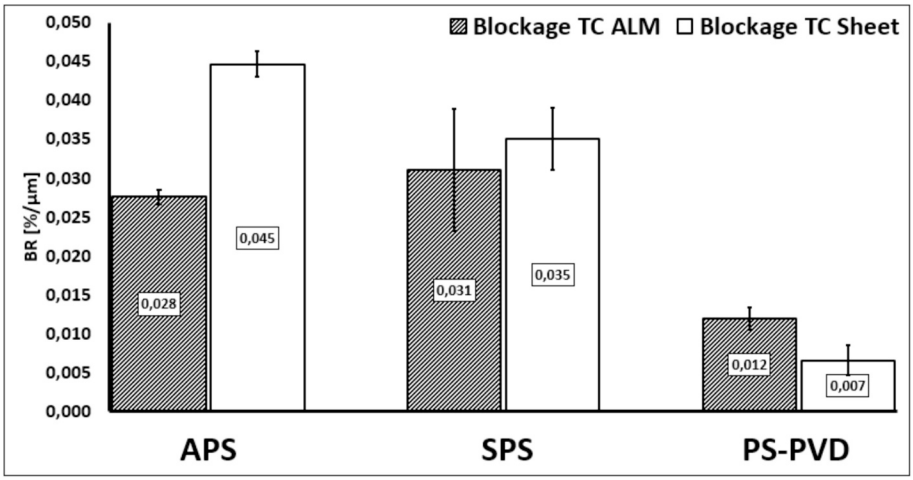

Fig. 8. Blocking ratio (BR) for APS, SPS and PS-PVD TBC systems on the ALM and Sheet samples.

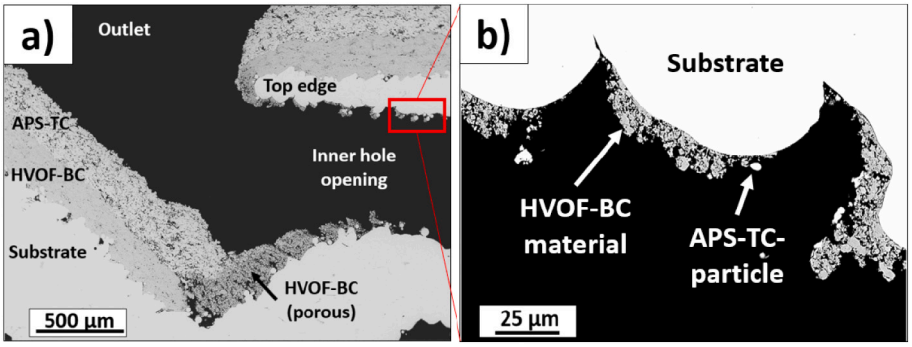

Fig. 9. APS microstructure within the pocket structure and b) within the inner cooling hole area.

Table 5
Average properties of the SPS columns along the edge of the cooling hole (Figs. 10 and 11), with the values taken in 500-micron steps for the ALM and the sheet sample starting from the outlet area (defined in Figs. 2 and 3).

ALM					
Outlet – pocket (µm)	0	500	1000	1500	2000
Spraying angle (°)	90	69	56	50	46
Growth angle (°)	90	85	78	63	59
Coating thickness (µm)	378	342	313	239	149

Sheet					
Outlet – inner hole opening (µm)	0	500	1000	1500	2000
Spraying angle (°)	70	70	70	70	70
Growth angle (°)	90	90	90	70	68
Coating thickness (µm)	470	462	439	389	316

plasma gas flow and were deflected into the inner cooling hole area. These un-melted/resolidified particles are also frequently found in inter-pass porosity bands or between columns, as described in literature [54–56]. The term "overspray" or "dust" is used in [55] to refer to these particles, which move in the outer zone of the plasma gas flow and are deposited in the coating during each pass.

On the sheet samples, the columns were able to grow along the entire length of the cooling hole on the bottom side, even on areas without a bond coat, as shown in Fig. 11. The growth angle of the columns varied from 90° to 70° near the hole opening and to 40° in the inner hole area, although the spraying angle remaining constant at 70°, refer to Table 5 and Fig. 11. This variation can be due to the shadowing effect of the right side of the cooling hole and the deflected gas flow, transporting the material into the inner hole area.

c) Microstructure and cooling hole blockage from the PS-PVD process

The low overall blocking ratio was due to limited material deposition in the outlet area and negligible deposition in the inner hole area, as shown in the SEM images in Figs. 7e) and 12a). The size of the columns decreased by 96 % from outside the hole to the center of the pocket. There the coating ended as a ten-micron thick layer, as shown in Fig. 12c). The columns that formed grew all at a 90-degree angle relative to the bond coat surface. Micron-sized particles that were partially melted and not vaporized were transported into the inner hole area. These particles were similar to SPS but larger in size and less in quantity, as illustrated in Fig. 12b). This is probably due to the high enthalpy and focused argon-helium plasma gas flow, combined with the low powder feed rate, which allowed a high degree of vaporization [57]. The vaporized material or clusters that form subsequently may follow the plasma gas flow, which gets deflected in front of the substrate [58]. According to He et al. [59] the growth of the PS-PVD coating begins with the nucleation and equiaxial growth of randomly oriented grains on the bond coat surface. Subsequently, gaseous material, such as atoms, molecules, or clusters in the nanometer range deposit. In later stages the growth is primally influenced by competitive and preferential growth of individual grains. This growth is controlled by shadowing effects, surface diffusion and bulk diffusion [59]. These stages ultimately determine the microstructure of the PS-PVD top coats. As the coating in the pocket is only a few tens of microns thick it is possible that the coating is in an early stage of the growth with small columns formed on asperities, which is the rough bond coat. The height of the columns increased and the microstructure of the coating became more feathery-like as the flat surface was approached. This can be explained by the higher nucleation

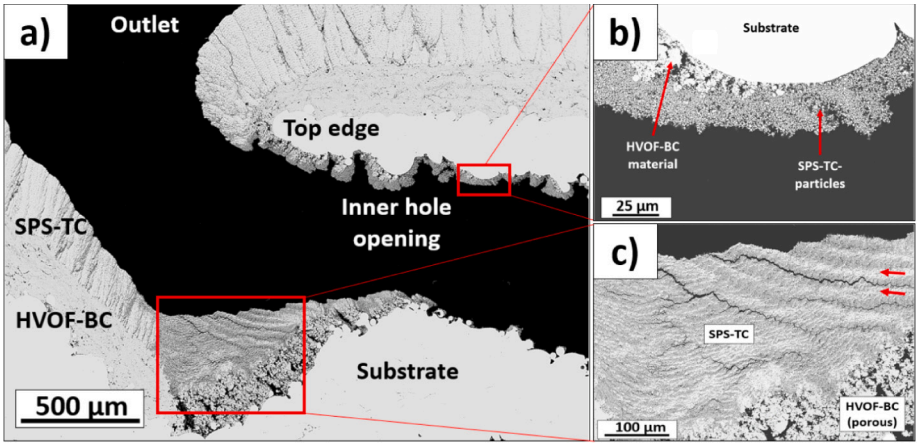

Fig. 10. SPS microstructure within the pocket structure b) Spherical particles deposited at the inner hole c) SPS TC within the pocket structure with alternating layers of porous and denser layers (marked with arrows).

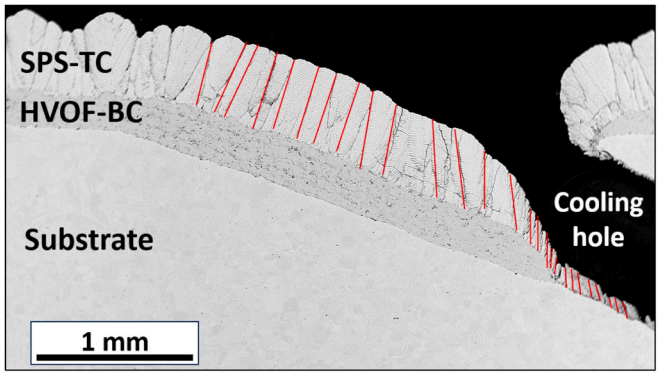

Fig. 11. SPS TC inside the cooling hole of the sheet sample with the columns marked in red.

rate and surface temperatures on the flat surfaces. Furthermore, the high temperature and viscosity of the plasma jet can cause the formation of a relatively thick boundary layer [60] as given by Eq. (1). Most of the material was likely deflected in front of the cooling holes due to the expanded plasma gas flow being much larger than the cooling holes and substrate, allowing it to flow around them more easily.

The growth of the columns was more pronounced on the back side of the samples, as shown in Fig. 7e). This phenomenon can be attributed to the non-line-of-sight property of the process and possible flow separation at the substrate edges. This is due to pressure drag and the subsequent formation of eddies behind the sample, which led to the transport of the vapor phase and the growth of columns in this area.

Similarly, the thin top coat layer in the cooling hole was observed for the sheet sample presented in Fig. 13. The thick bond coat, which could not be polished, obstructed the hole opening, reduced the hole diameter, and thus limited the transport of vaporized material into the inner hole area. The proximity of the shallow outlet area to the flat surface may promote the growth of the columns, as they become larger.

4. Conclusion and outlook

In this experimental study HVOF bond coats and three different top coat spraying methods were tested on substrates with complex and conventional cooling hole geometries to investigate the blockage. It was found that already the bond coat spraying leads to significant blockage, due to splashing of impacting particles. When comparing the different deposition methods, the PS-PVD process showed the best results in terms of avoiding blockage for both hole geometries. This was attributed to the deflected gas flow in front of the cooling holes that lead to limited deposition of atomized species or clusters at the coatings within the cooling holes. The different particle sizes of the feedstock and gas flow properties seemed to influence the location of deposition in the cooling holes. The large APS particles were deposited in line-of sight and blocked the outlet area. This type of blockage was reduced for example in case of the complex cooling hole geometry, with its concave pocket structure, as it was filled instead of assembling in front of the hole opening. The sub-micron particles in the case of SPS were able to follow the gas flow in the cooling holes and deposited in the inner cooling hole area, resulting in increased blockage. Future research can aim to simulate and comprehend the impact of substrate and cooling hole geometry on gas flow and particle trajectories.

Funding

This research project was financially supported within the framework of LuFo by the Federal Republic of Germany, Federal Ministry for Economic Affairs and Climate Action, according to a decision of the

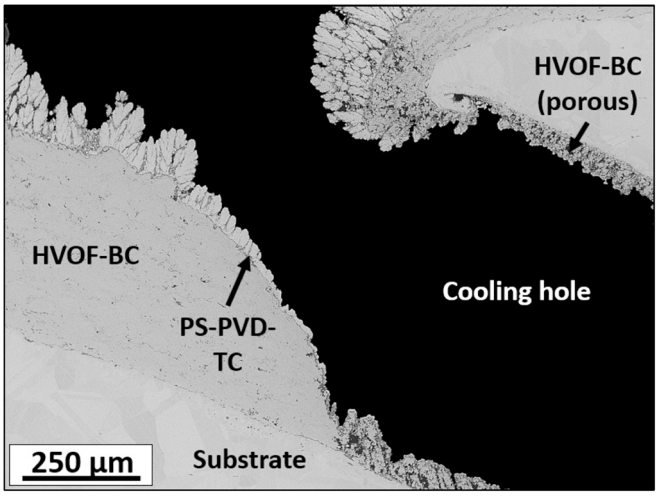

Fig. 13. Reduced growth of the PS-PVD top coat within the fan shaped hole of the sheet sample.

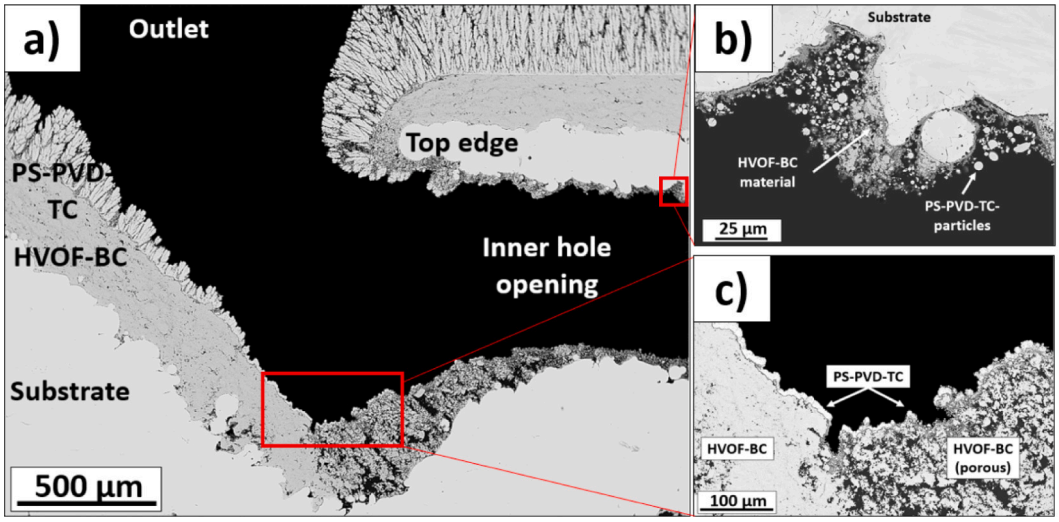

Fig. 12. SEM images showing the PS-PVD coating within the pocket structure b) Deposition of spherical YSZ-particles in the inner cooling hole area and c) Thin PS-PVD top coat layer formed in the center of the pocket.

German Bundestag (FKZ: 20T1702) as well as by Rolls-Royce Deutschland Ltd & Co KG. The technical and financial support is appreciated.

CRediT authorship contribution statement

Martin Rüßmann: Writing – original draft, Visualization, Validation, Methodology, Investigation, Formal analysis, Data curation, Conceptualization. **Emine Bakan:** Writing – review & editing, Methodology, Investigation, Conceptualization. **Susanne Schrüfer:** Writing – review & editing, Validation, Resources, Methodology, Conceptualization. **Olivier Guillon:** Writing – review & editing. **Robert Vaßen:** Writing – review & editing, Validation, Supervision, Methodology, Conceptualization.

Declaration of competing interest

The authors declare that they have no known competing financial interests or personal relationships that could have appeared to influence the work reported in this paper.

Data availability

No data was used for the research described in the article.

Acknowledgements

The authors would like to thank Frank Kurze, Karl-Heinz Rauwald and Ralf Laufs for their assistance in operating the spraying facilities. Furthermore, we extend our appreciation to Georg Mauer for discussions regarding the different thermal spray methods.

References

[1] N.P. Padture, Advanced structural ceramics in aerospace propulsion, Nat. Mater. 15 (8) (2016) 804–809, https://doi.org/10.1038/nmat4687.
[2] T. Beck, Laser drilling in gas turbine blades: shaping of holes in ceramic and metallic coatings, Laser Tech. J. 8 (3) (2011) 40–43, https://doi.org/10.1002/latj.201190024.
[3] S.S. Babu, N. Raghavan, J. Raplee, S.J. Foster, C. Frederick, M. Haines, R.R. Dehoff, Additive manufacturing of nickel superalloys: opportunities for innovation and challenges related to qualification, Metall. Mater. Trans. A 49 (2018) 3764–3780, https://doi.org/10.1007/s11661-018-4702-4.
[4] S. Sanchez, P. Smith, Z. Xu, G. Gaspard, C.J. Hyde, W.W. Wits, A.T. Clare, Powder Bed Fusion of nickel-based superalloys: a review, Int. J. Mach. Tools Manuf. 165 (2021) 103729, https://doi.org/10.1016/j.ijmachtools.2021.103729.
[5] R.S. Bunker, Effect of partial coating blockage on film cooling effectiveness, in: Turbo Expo: Power for Land, Sea, and Air vol. 78569, American Society of Mechanical Engineers, May 2000, https://doi.org/10.1115/2000-GT-0244 (p. V003T01A051).
[6] P. Cheng-xiong, Z. Jing-zhou, H. Ke-nan, Numerical investigation of partial blockage effect on film cooling effectiveness, Math. Probl. Eng. 2014 (2014), https://doi.org/10.1155/2014/167193.
[7] J. Kim, M.G. Dunn, A.J. Baran, D.P. Wade, E.L. Tremba, Deposition of Volcanic Materials in the Hot Sections of Two Gas Turbine Engines, 1993, https://doi.org/10.1115/1.2906754.
[8] C. Guinard, G. Montay, V. Guipont, M. Jeandin, J. Girardot, M. Schneider, Residual stress analysis of laser-drilled thermal barrier coatings involving various bond coats, J. Therm. Spray Technol. 24 (2015) 252–262, https://doi.org/10.1007/s11666-014-0185-z.
[9] E. Jerby, A.M. Thompson, Microwave drilling of ceramic thermal-barrier coatings, J. Am. Ceram. Soc. 87 (2) (2004) 308–310, https://doi.org/10.1111/j.1551-2916.2004.00308.x.
[10] K.T. Voisey, T.W. Clyne, Laser drilling of cooling holes through plasma sprayed thermal barrier coatings, Surf. Coat. Technol. 176 (3) (2004) 296–306, https://doi.org/10.1016/S0257-8972(03)00748-5.
[11] C. Gao, Z. Liu, Y. Qiu, K. Zhao, Feasibility of drilling holes on thermal barrier coated superalloy using electrical-discharge machining, Procedia CIRP 95 (2020) 522–526, https://doi.org/10.1016/j.procir.2020.02.259.
[12] R. Vaßen, M.O. Jarligo, T. Steinke, D.E. Mack, D. Stöver, Overview on advanced thermal barrier coatings, Surf. Coat. Technol. 205 (4) (2010) 938–942, https://doi.org/10.1016/j.surfcoat.2010.08.151.
[13] R. Vassen, A. Stuke, D. Stöver, Recent developments in the field of thermal barrier coatings, J. Therm. Spray Technol. 18 (2009) 181–186, https://doi.org/10.1007/s11666-009-9312-7.
[14] T.S. Sidhu, S. Prakash, R.D. Agrawal, Studies on the properties of high-velocity oxy-fuel thermal spray coatings for higher temperature applications, Mater. Sci. 41 (2005) 805–823, https://doi.org/10.1007/s11003-006-0047-z.
[15] B. Rajasekaran, G. Mauer, R. Vaßen, Enhanced characteristics of HVOF-sprayed MCrAlY bond coats for TBC applications, J. Therm. Spray Technol. 20 (6) (2011) 1209–1216, https://doi.org/10.1007/s11666-011-9668-3.
[16] E. Bakan, R. Vaßen, Ceramic top coats of plasma-sprayed thermal barrier coatings: materials, processes, and properties, J. Therm. Spray Technol. 26 (2017) 992–1010, https://doi.org/10.1007/s11666-017-0597-7.
[17] N.P. Padture, M. Gell, E.H. Jordan, Thermal barrier coatings for gas-turbine engine applications, Science 296 (5566) (2002) 280–284. https://www.science.org/doi/10.1126/science.1068609.
[18] P.L. Fauchais, J.V. Heberlein, M.I. Boulos, Thermal Spray Fundamentals: From Powder to Part, Springer Science & Business Media, 2014.
[19] S. Kuroda, Y. Tashiro, H. Yumoto, S. Taira, H. Fukanuma, S. Tobe, Peening action and residual stresses in high-velocity oxygen fuel thermal spraying of 316L stainless steel, J. Therm. Spray Technol. 10 (2001) 367–374, https://doi.org/10.1361/105996301770349457.
[20] C.A. Whitfield, R.P. Schroeder, K.A. Thole, S.D. Lewis, Blockage effects from simulated thermal barrier coatings for cylindrical and shaped cooling holes, J. Turbomach. 137 (9) (2015) 091004, https://doi.org/10.1115/1.4029879.
[21] R. Gadow, M. Floristán, Manufacturing engineering in thermal spraying by advanced robot systems and process kinematics, in: Future Development of Thermal Spray Coatings, Woodhead Publishing, 2015, pp. 259–280, https://doi.org/10.1016/B978-0-85709-769-9.00011-7.
[22] A. Candel, Entwicklung von thermisch gespritzten Schichtverbundwerkstoffen durch Optimierung geeigneter robotergestützter Brennerbewegungsabläufe, Shaker Verlag GmbH, Aachen, 2009.
[23] M. Floristán, J.A. Montesinos, J.A. García-Marín, A. Killinger, R. Gadow, Robot trajectory planning for high quality thermal spray coating processes on complex shaped components, in: International Thermal Spray Conference vol. 83720, ASM International, May 2012, pp. 448–453, https://doi.org/10.31399/asm.cp.itsc2012p0448.
[24] A. Candel, R. Gadow, Trajectory generation and coupled numerical simulation for thermal spraying applications on complex geometries, J. Therm. Spray Technol. 18 (2009) 981–987, https://doi.org/10.1007/s11666-009-9338-x.
[25] R. Vaßen, E. Bakan, D.E. Mack, O. Guillon, A perspective on thermally sprayed thermal barrier coatings: current status and trends, J. Therm. Spray Technol. 31 (4) (2022) 685–698, https://doi.org/10.1007/s11666-022-01330-2.
[26] K. Von Niessen, M. Gindrat, Plasma spray-PVD: a new thermal spray process to deposit out of the vapor phase, J. Therm. Spray Technol. 20 (2011) 736–743, https://doi.org/10.1007/s11666-011-9654-9.
[27] B.J. Harder, D. Zhu, M.P. Schmitt, D.E. Wolfe, Microstructural effects and properties of non-line-of-sight coating processing via plasma spray-physical vapor deposition, J. Therm. Spray Technol. 26 (2017) 1052–1061, https://doi.org/10.1007/s11666-017-0570-5.
[28] Z. Tang, H. Kim, I. Yaroslavski, G. Masindo, Z. Celler, D. Ellsworth, Novel thermal barrier coatings produced by axial suspension plasma spray, in: Proceedings of International Thermal Spray Conference and Exposition, September 2011, pp. 593–597, https://doi.org/10.1007/s11666-017-0570-5.
[29] B. Bernard, A. Quet, L. Bianchi, V. Schick, A. Joulia, A. Malié, B. Rémy, Effect of suspension plasma-sprayed YSZ columnar microstructure and bond coat surface preparation on thermal barrier coating properties, J. Therm. Spray Technol. 26 (6) (2017) 1025–1037, https://doi.org/10.1007/s11666-017-0584-z.
[30] G. Mauer, R. Vaßen, Coatings with columnar microstructures for thermal barrier applications, Adv. Eng. Mater. 22 (6) (2020) 1900988, https://doi.org/10.1002/adem.201900988.
[31] H. Martin, Heat and mass transfer between impinging gas jets and solid surfaces, in: Advances in Heat Transfer vol. 13, Elsevier, 1977, pp. 1–60, https://doi.org/10.1016/S0065-2717(08)70221-1.
[32] K. Pourang, C. Moreau, A. Dolatabadi, Effect of substrate and its shape on in-flight particle characteristics in suspension plasma spraying, J. Therm. Spray Technol. 25 (2016) 44–54, https://doi.org/10.1007/s11666-015-0342-z.
[33] A. Dolmaire, S. Goutier, A. Joulia, P.M. Geffroy, M. Vardelle, L. Bianchi, Experimental study of the impact of substrate shape and tilting on particle velocity in suspension plasma spraying, J. Therm. Spray Technol. 29 (2020) 358–367, https://doi.org/10.1007/s11666-019-00977-8.
[34] Z.U. Ahmed, Y.M. Al-Abdeli, F.G. Guzzomi, Impingement pressure characteristics of swirling and non-swirling turbulent jets, Exp. Thermal Fluid Sci. 68 (2015) 722–732, https://doi.org/10.1016/j.expthermflusci.2015.07.017.
[35] A. Dolmaire, S. Goutier, M. Vardelle, P.M. Geffroy, A. Joulia, Investigations on particle behavior at the stagnation zone for a suspension particle jet in plasma spray conditions, J. Therm. Spray Technol. 30 (2021) 1001–1014, https://doi.org/10.1007/s11666-021-01174-2.
[36] J. Anderson, Fundamentals of Aerodynamics, 6th edition, McGraw-Hill, NY, 2007.
[37] T. Kiełczawa, P. Sokołowski, A. Małachowska, The influence of substrate topography on the plasma jet flow in the substrate boundary layer under suspension plasma spray conditions: a numerical approach, J. Therm. Spray Technol. 31 (1–2) (2022) 84–101, https://doi.org/10.1007/s11666-022-01336-w.
[38] G. Mauer, A. Hospach, R. Vaßen, Process development and coating characteristics of plasma spray-PVD, Surf. Coat. Technol. 220 (2013) 219–224, https://doi.org/10.1016/j.surfcoat.2012.08.067.
[39] K. Von Niessen, M. Gindrat, Plasma spray-PVD: a new thermal spray process to deposit out of the vapor phase, J. Therm. Spray Technol. 20 (2011) 736–743, https://doi.org/10.1007/s11666-011-9654-9.

[40] G. Mauer, Plasma characteristics and plasma-feedstock interaction under PS-PVD process conditions, Plasma Chem. Plasma Process. 34 (2014) 1171–1186, https://doi.org/10.1007/s11090-014-9563-z.
[41] G. Mauer, R. Vaßen, Conditions for nucleation and growth in the substrate boundary layer at plasma spray-physical vapor deposition (PS-PVD), Surf. Coat. Technol. 371 (2019) 417–427, https://doi.org/10.1016/j.surfcoat.2018.06.086.
[42] A. Hospach, Untersuchung zum Thin Film Low Pressure Plasma Spraying (LPPS-TF) Prozess (No. PreJuSER-22357), Werkstoffsynthese und Herstellverfahren, 2012.
[43] K. Von Niessen, M. Gindrat, A. Refke, Vapor phase deposition using plasma spray-PVD™, J. Therm. Spray Technol. 19 (2010) 502–509, https://doi.org/10.1007/s11666-009-9428-9.
[44] A. Vardelle, C. Moreau, J. Akedo, H. Ashrafizadeh, C.C. Berndt, J.O. Berghaus, P. Vuoristo, The 2016 thermal spray roadmap, J. Therm. Spray Technol. 25 (2016) 1376–1440, https://doi.org/10.1007/s11666-016-0473-x.
[45] S. Rezanka, Abscheidung von Wärmedämmschichtsystemen mit dem Plasma Spray-Physical Vapor Deposition-(PS-PVD-) Prozess-Untersuchung des Prozesses und der hergestellten Schichten (No. FZJ-2015-07483), Werkstoffsynthese und Herstellungsverfahren, 2015.
[46] S. Rezanka, G. Mauer, R. Vaßen, Improved thermal cycling durability of thermal barrier coatings manufactured by PS-PVD, J. Therm. Spray Technol. 23 (2014) 182–189, https://doi.org/10.1007/s11666-013-9971-2.
[47] B. Zheng, J.C. Haley, N. Yang, J. Yee, K.W. Terrassa, Y. Zhou, J.M. Schoenung, On the evolution of microstructure and defect control in 316L SS components fabricated via directed energy deposition, Mater. Sci. Eng. A 764 (2019) 138243, https://doi.org/10.1016/j.msea.2019.138243.
[48] S. Pandey, R. Srivastava, R. Narain, Study on the effect of powder feed rate on direct metal deposition layer of precipitation hardened steel, Mater. Today Proc. 26 (2020) 2272–2276, https://doi.org/10.1016/j.matpr.2020.02.492.
[49] V. Katranidis, S. Gu, B. Allcock, S. Kamnis, Experimental study of high velocity oxy-fuel sprayed WC-17Co coatings applied on complex geometries. Part A: influence of kinematic spray parameters on thickness, porosity, residual stresses and microhardness, Surf. Coat. Technol. 311 (2017) 206–215, https://doi.org/10.1016/j.surfcoat.2017.01.015.
[50] W. Tillmann, E. Vogli, B. Krebs, Influence of the spray angle on the characteristics of atmospheric plasma sprayed hard material based coatings, J. Therm. Spray Technol. 17 (2008) 948–955, https://doi.org/10.1007/s11666-008-9261-6.
[51] W. Uczak de Goes, N. Markocsan, M. Gupta, Microstructural changes in suspension plasma-sprayed TBCs deposited on complex geometry substrates, Coatings 10 (7) (2020) 699, https://doi.org/10.3390/coatings10070699.
[52] A. Ganvir, R.F. Calinas, N. Markocsan, N. Curry, S. Joshi, Experimental visualization of microstructure evolution during suspension plasma spraying of thermal barrier coatings, J. Eur. Ceram. Soc. 39 (2–3) (2019) 470–481, https://doi.org/10.1016/j.jeurceramsoc.2018.09.023.
[53] F. Caio, C. Moreau, Influence of substrate shape and roughness on coating microstructure in suspension plasma spray, Coatings 9 (11) (2019) 746, https://doi.org/10.3390/coatings9110746.
[54] K. VanEvery, M.J. Krane, R.W. Trice, H. Wang, W. Porter, M. Besser, J. Almer, Column formation in suspension plasma-sprayed coatings and resultant thermal properties, J. Therm. Spray Technol. 20 (2011) 817–828, https://doi.org/10.1007/s11666-011-9632-2.
[55] B. Bernard, L. Bianchi, A. Malié, A. Joulia, B. Rémy, Columnar suspension plasma sprayed coating microstructural control for thermal barrier coating application, J. Eur. Ceram. Soc. 36 (4) (2016) 1081–1089, https://doi.org/10.1016/j.jeurceramsoc.2015.11.018.
[56] J. Joeris, A. Tiwari, S. Brinckmann, F. Kurze, O. Guillon, R. Vaßen, Evaluation of major factors influencing the TBC topcoat formation in axial suspension plasma spraying (SPS), Int. J. Appl. Ceram. Technol. 20 (2) (2023) 884–895, https://doi.org/10.1111/ijac.14288.
[57] G. Mauer, A. Hospach, R. Vaßen, Process development and coating char-acteristics of plasma spray-PVD, Surf. Coat. Technol. 220 (2013) 219–224, https://doi.org/10.1016/j.surfcoat.2012.08.067.
[58] P. Wang, Numerical Simulation of Plasma Spray-Physical Vapor Deposition (No. FZJ-2017-08316), Werkstoffsynthese und Herstellungsverfahren, 2017.
[59] W. He, G. Mauer, Y.J. Sohn, A. Schwedt, O. Guillon, R. Vaßen, Investigation on growth mechanisms of columnar structured YSZ coatings in Plasma Spray-Physical Vapor Deposition (PS-PVD), J. Eur. Ceram. Soc. 39 (10) (2019) 3129–3138, https://doi.org/10.1016/j.jeurceramsoc.2019.04.003.
[60] G. Mauer, Numerical study on particle–gas interaction close to the substrates in thermal spray processes with high-kinetic and low-pressure conditions, J. Therm. Spray Technol. 28 (1–2) (2019) 27–39, https://doi.org/10.1007/s11666-018-0810-3.